



# Incorporation of CoO nanoparticles in 3D marigold flower-like hierarchical architecture MnCo<sub>2</sub>O<sub>4</sub> for highly boosting solar light photo-oxidation and reduction ability

Jianhua Zheng, Lei Zhang\*

College of Chemistry, Liaoning University, 66 Chongshan Middle Road, Shenyang, Liaoning, 110036, People's Republic of China



## ARTICLE INFO

**Keywords:**  
Photocatalytic degradation  
CoO@MnCo<sub>2</sub>O<sub>4</sub>  
p-n Heterostructure  
Tetracycline  
Hexavalent chromium

## ABSTRACT

Most previous reported photocatalysts designs show that, either photocatalytic oxidation (PCO) or reduction (PCR) is inhibited due to the insufficient govern of the photo-excited  $h^+$  and  $e^-$ . To overcome this problem, we consider that both PCO and PCR could be improved simultaneously by employing suitable photocatalyst. Herein, the novel 3D marigold flower-like hierarchical architecture CoO@MnCo<sub>2</sub>O<sub>4</sub> was successfully synthesized by anchoring CoO nanoparticles (NPs) on MnCo<sub>2</sub>O<sub>4</sub> flower using a facile solvothermal method followed thermal annealing treatment under N<sub>2</sub> atmosphere for the first time. This strategy relies on the formation of a p-n heterostructure with matching energy band gaps, in which CoO NPs tightly adhere to the surface of hierarchical MnCo<sub>2</sub>O<sub>4</sub> microflowers, and the flower-like MnCo<sub>2</sub>O<sub>4</sub> act as scaffold to disperse CoO NPs. The as-fabricated CoO@MnCo<sub>2</sub>O<sub>4</sub> hybrid not only presented remarkable performance for PCO of tetracycline (TC) but also exhibited excellent PCR of hexavalent chromium (Cr (VI)) under visible light irradiation. Meanwhile, the photocatalyst also can be used for treatment a mixture of them and exhibited promoted photocatalytic efficiency. That's the primary reason that  $h^+$  and  $e^-$  can play their own roles to accomplish PCO and PCR, respectively. Moreover, the unique 3D hierarchical microflowers structure not only provide a higher specific surface area, sufficient active sites and enhanced light harvesting, but also significantly decrease the aggregation of CoO particles. The appearance photocatalytic mechanism of the p-n heterostructure system was also discussed in detail. The facile synthesis strategy and outstanding photocatalytic performance make the 3D hierarchical architecture CoO@MnCo<sub>2</sub>O<sub>4</sub> a promising candidate as a visible light photocatalyst.

## 1. Introduction

In recent years, the removal of toxic contaminants, such as heavy metals, organic dyes and antibiotics, arising from industrial and municipal wastewaters, has been always a huge challenge as the deterioration of global environment is increasing [1–3]. Therefore, searching for strategies utilizing low cost, renewable, and clean form of energy to removal of these harmful environmental contaminants is urgently needed. In this regard, photocatalysis using semiconductors has attracted wide attention for it is more effective and environmental benignity. Successful implementation of the technology hinges on the development of high active and durable photocatalysts. Nowadays, some of photocatalysts that is sensitive to visible light (such as Ag/Ag<sub>3</sub>PO<sub>4</sub>/BiVO<sub>4</sub>/RGO [4] and AgI/BiVO<sub>4</sub> [5]) have been employed and exhibited a higher photocatalytic efficiency to degradation of tetracycline. However, the noble metals-based catalysts possess the high cost and scarcity, which greatly restricts their widespread applications.

Transition metal oxides (TMOs) are recognized as the most probable alternatives to noble metal-based catalysts. This creates a tremendous deal of interest in exploring of novel and efficient photocatalytic materials [6–10].

Among the reported semiconductors, spinel complex oxides transition-metal oxides (AB<sub>2</sub>O<sub>4</sub>), such as ZnFe<sub>2</sub>O<sub>4</sub> [11–13], CoFe<sub>2</sub>O<sub>4</sub> [14,15], MnFe<sub>2</sub>O<sub>4</sub> [16,17], CoMn<sub>2</sub>O<sub>4</sub> [18,19], ZnMn<sub>2</sub>O<sub>4</sub> [20,21], NiCo<sub>2</sub>O<sub>4</sub> [22,23], ZnCo<sub>2</sub>O<sub>4</sub> [24,25] and CuCo<sub>2</sub>O<sub>4</sub> [26], have been considered as the most promising class of catalysts for photocatalytic removal contaminants, the energy conversion, oxygen reduction reaction, supercapacitor and lithium-ion batteries. The complex chemical compositions as well as the synergic effects of various metal elements in these materials result in their superior photoelectrochemical activity. Among them, n-type MnCo<sub>2</sub>O<sub>4</sub> possess attractive narrow band gap, high catalytic activity, super chemical stability and environmental friendliness. These unique merits make it serve as a promising candidate for visible-light responsive photocatalytic application. Such as, Wang's group have

\* Corresponding author.

E-mail address: [zhanglei63@126.com](mailto:zhanglei63@126.com) (Z. Lei).

developed  $\text{MnCo}_2\text{O}_4$  microspheres as a heterogeneous co-catalyst for photocatalytic  $\text{CO}_2$  reduction with visible light [27]. Shibli et al. obtained octahedrally shaped  $\text{MnCo}_2\text{O}_4$  catalyst particles for the application in photocatalytic water splitting reaction [28]. However, the lower charge separation rate and unsatisfactory visible-light absorption of pure  $\text{MnCo}_2\text{O}_4$  limit its application and urgently call for further improvement of  $\text{MnCo}_2\text{O}_4$  to overcome these shortcomings. A well-accepted approach to solve the problem is to construct heterojunctions by coupling  $\text{MnCo}_2\text{O}_4$  with other semiconductors. Recently, some  $\text{MnCo}_2\text{O}_4$ -based heterojunctions including  $\text{NiCo}_2\text{O}_4/\text{MnCo}_2\text{O}_4$  [29],  $\text{CuCo}_2\text{O}_4/\text{MnCo}_2\text{O}_4$  [30],  $\text{MnO}_2/\text{MnCo}_2\text{O}_4/\text{Ni}$  [31], MWCNT/ $\text{MnCo}_2\text{O}_4$  [32] and  $\text{MnCo}_2\text{O}_4/\text{N}$ , S-CNT [33], have been developed and the fabrication of  $\text{MnCo}_2\text{O}_4$ -based heterojunctions can markedly boost the catalytic activity by realizing the interfacial charge transfer between components, thus restraining the recombination of  $e^-/h^+$  pairs.

P-type semiconductor CoO with highly efficient visible light photocatalytic performance has been extensively studied for energy conversion devices due to the narrow energy bandgap (2.2–2.6 eV). Very recently, our group have reported a novel CoO/ $\text{CoSnO}_3$  heterojunction [34], and this heterojunction exhibited an excellent photoelectrocatalytic activity than its single components. However, to the best of our knowledge, CoO@ $\text{MnCo}_2\text{O}_4$  heterojunctions have not been reported in the literatures on the photocatalytic properties. Thus, the development of CoO@ $\text{MnCo}_2\text{O}_4$  heterojunctions possessing a staggered band-bip type for superior photocatalytic activity is highly desirable and anticipated.

Based on the above considerations, the 3D marigold flower-like hierarchical CoO@ $\text{MnCo}_2\text{O}_4$  photocatalyst was constructed. Our strategy was to decorate CoO nanoparticles on the nanoleaf of marigold flower-like  $\text{MnCo}_2\text{O}_4$  to form 3D hierarchical architecture CoO@ $\text{MnCo}_2\text{O}_4$  for enhancing light absorption, which can act as carrier sinks, produce more catalytic sites, and facilitate the mass transfer of reactants. The 3D CoO@ $\text{MnCo}_2\text{O}_4$  hybrids displayed remarkable improved photocatalytic activity towards the PCO of TC and PCR of Cr (VI), which are typical antibiotics and heavy metal contaminants in the wastewater, owing to the formation of a p-n junction. Moreover, the possible mechanism was also proposed.

## 2. Experimental

### 2.1. Materials

The reagents and solvents used were of analytical reagent grade and used without further purification.

### 2.2. Preparation of photocatalysts

Firstly, the 3D hierarchical  $\text{MnCo}_2\text{O}_4$  marigold flowers were synthesized by a solvothermal method followed by calcinations. Typically, 0.245 g Manganese acetate tetrahydrate and 0.498 g Cobalt acetate tetrahydrate were added into 80 mL of ethylene glycol containing 1 mL deionized water to obtain a transparent solution under magnetic stirring. Then 0.219 g polyvinyl pyrrolidone ( $M_w = 10,000 \text{ g mol}^{-1}$ ) was added into the above solution. The obtained mixture was transferred into Teflon-lined autoclave and maintained at 180 °C for 12 h. The precipitate was collected, washed with ultrapure water and ethanol for several times, and dried at 80 °C overnight. The as-prepared precursor was annealed at 500 °C in the air for 4 h with the heating rate of 2 °C  $\text{min}^{-1}$ . For the synthesis of CoO@ $\text{MnCo}_2\text{O}_4$  (the mass ratio of CoO and  $\text{MnCo}_2\text{O}_4$  is about 1:10), 0.50 g  $\text{MnCo}_2\text{O}_4$  was immersed in 40 mL of methanol solution containing 0.175 g of  $\text{Co}(\text{CH}_3\text{COO})_2 \cdot 4\text{H}_2\text{O}$  for 24 h with continuous stirring. After volatilization of methanol, the prepared mixture was dried in oven at 80 °C overnight. Finally, the dried powder was calcinated at 400 °C for 3 h in an  $\text{N}_2$  atmosphere, with a heating rate of 2 °C/min (Scheme 1). Meanwhile, the molar ration of  $\text{Co}^{2+}$  and  $\text{Co}^{3+}$  was determined according to reported [35]. Additionally, pure

CoO nanoparticles were synthesized by the similar processes without the addition of  $\text{MnCo}_2\text{O}_4$ .

### 2.3. Characterization methods

Field emission scanning electron microscope (SEM, S4800, Hitachi Co., Japan); Transmission electron microscope (TEM, 2100F, JEOL Co., Japan) and high resolution transmission electron microscopy (HRTEM, 2100F, JEOL Co., Japan); X-ray diffraction with Cu Ka radiation (XRD, D/max-2200, Rigaku., Japan) was used to determine the crystal structure and purity of samples. X-ray photoelectron spectroscopic (XPS, Thermo Electron, ESCALAB 250 Xi., USA). UV-vis diffuses reflectance spectra (DRS, Shimadzu, UV-2600). TOC was measured by multi N/C 3100 (Analytik Jena, Germany).

### 2.4. Photocatalytic activity measurements

#### 2.4.1. Photocatalysis of TC degradation and Cr(VI) reduction

Photocatalytic properties of catalysts were tested in the decomposition of organic pollutant tetracycline (TC, 10 mg/L) and reduction of aqueous Cr (VI) ( $\text{K}_2\text{Cr}_2\text{O}_7$  aqueous solution, 10 mg/L), using a 500 W Xeon lamp as exciting source,  $\lambda > 420 \text{ nm}$ . Before irradiation, 50 mL TC or Cr (VI) aqueous containing of 50 mg catalyst was continuous stirred for 60 min in dark to obtain the adsorption-desorption equilibrium of catalyst and pollution. During illumination, 3 mL of mixture aqueous was taken at an interval of 30 min. The concentration of TC or Cr (VI) was determined by a UV-vis spectrophotometer.

#### 2.4.2. Simultaneous photocatalysis of TC/Cr(VI)

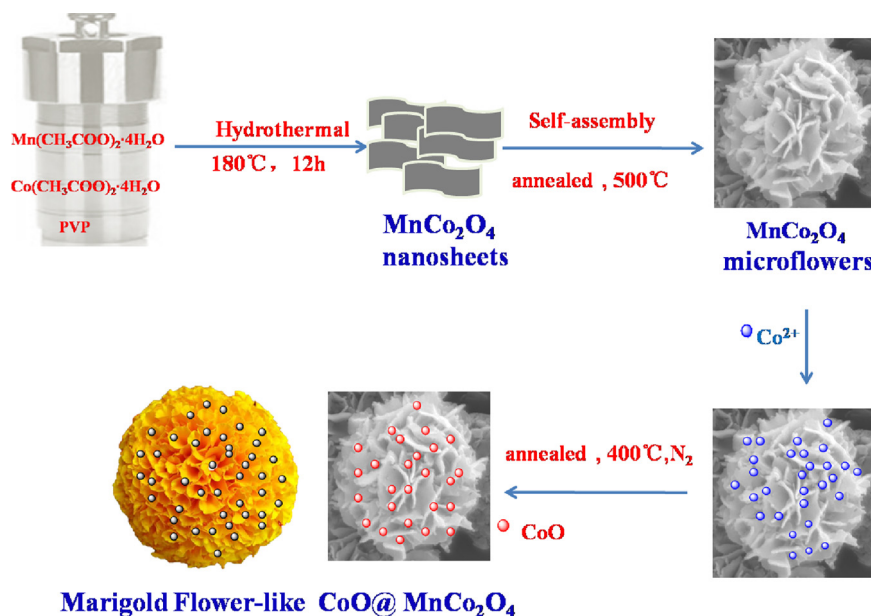
Experimentally, the concentrations of TC/Cr (VI) were monitored using HPLC (LC-16 system)/UV-vis spectrophotometer (diphenylcarbazide method), respectively. The HPLC was equipped with a SB-C<sub>18</sub> column using SPD-16 UV-vis detector at 272 nm. The mobile phase was 75:25 (v/v) oxalic acid (0.01 mol  $\text{L}^{-1}$ ) and acetonitrile (0.7 mL  $\text{min}^{-1}$ ).

## 3. Results and discussions

### 3.1. Characterization

The morphologies of pure  $\text{MnCo}_2\text{O}_4$ , and the as-prepared CoO@ $\text{MnCo}_2\text{O}_4$  composite were investigated via SEM and TEM. As shown in Fig. 1a, 3D marigold flower-like hierarchical architecture  $\text{MnCo}_2\text{O}_4$  microspheres (with diameters of 2.0–2.5  $\mu\text{m}$ ) were fabricated by numerous 2D interlaced nanosheets (with thicknesses of  $\sim 10 \text{ nm}$ ), which are aligned from the sphere center to the surface, constructing the hierarchical architecture with a large amount of open-free space. The unique structure can greatly enlarge the contact area between the target and CoO@ $\text{MnCo}_2\text{O}_4$ . Fig. 1b, c displays the SEM image of CoO@ $\text{MnCo}_2\text{O}_4$  hybrids, where CoO NPs are assemble on the surface of  $\text{MnCo}_2\text{O}_4$  nanoleafs, and did not affect the morphology of marigold flower-like  $\text{MnCo}_2\text{O}_4$ . From the TEM image (Fig. 1d), the enlarged view shows that CoO NPs with a diameter of  $\sim 10 \text{ nm}$  are tightly anchored on the surface of each leaf to form CoO@ $\text{MnCo}_2\text{O}_4$  heterojunction. The intimately contacted interface plays an important role for accelerating the separation of the photogenerated charge carriers. HRTEM image (Fig. 1e) displays a lattice interval of 0.24 nm, corresponding to (200) plane of CoO. Analogously, the lattice interval of 0.48 nm attributes to (111) lattice planes of  $\text{MnCo}_2\text{O}_4$ . Additionally, the intersection of the lattice fringe can be found in (indicated by the white circles), further confirming that the p-n junction was formed between CoO and  $\text{MnCo}_2\text{O}_4$ .

Fig. 1f displays the XRD patterns of pure  $\text{MnCo}_2\text{O}_4$ , CoO and CoO@ $\text{MnCo}_2\text{O}_4$  composite. The diffraction peaks of pure  $\text{MnCo}_2\text{O}_4$  located at  $2\theta = 18.55$  (111), 30.54 (220), 35.99 (311), 43.76 (400), 54.34 (422), 57.91 (511), 63.62 (440) and 75.30 (533), which are in accordance



Scheme 1. Illustration of the synthesis process of the  $\text{CoO}@\text{MnCo}_2\text{O}_4$  hybrids.

with the well-crystallized  $\text{MnCo}_2\text{O}_4$  with spinel structure (JCPDS No. 23-1237) [36]. As for the  $\text{CoO}$  sample, the main diffraction peaks observed at 20 values of 36.52 (111), 42.42 (200), 61.56 (220), and 73.61 (222) is well belong to the  $\text{CoO}$  (JCPDS No: 65-2902) [37]. For the  $\text{CoO}@\text{MnCo}_2\text{O}_4$  hybrid, the XRD patterns display a combination of the two sets of diffraction data for both  $\text{MnCo}_2\text{O}_4$  (marked by ♠) and  $\text{CoO}$  (marked by ♦). It is worth mentioning that the  $\text{CoO}@\text{MnCo}_2\text{O}_4$  hybrid exhibits relatively weak diffraction peaks of  $\text{CoO}$  due to the low content. There is no impure diffraction peak was observed, confirming that the formation of  $\text{CoO}@\text{MnCo}_2\text{O}_4$  hybrid.

X-ray photoelectron spectroscopy (XPS) was used to further insight into the elements information and valence states of surface elements in of as-prepared  $\text{CoO}@\text{MnCo}_2\text{O}_4$ . As Fig. 2a displayed, all the peaks ascribed to Mn, Co and O elements and no other impure peaks of elements were observed. The high-resolution spectra of Mn 2p, Co 2p and O 1s were exhibited in Fig. 2b–d. As Fig. 2b shown, the major peaks with binding energies at 652.89 and 641.10 eV are observed, which are corresponding to the  $\text{Mn}^{2+}$ ; while the other two peaks located at 654.3 and 642.65 eV are characteristic of  $\text{Mn}^{3+}$ , respectively. [38,39] For the spectra of Co 2p in  $\text{CoO}@\text{MnCo}_2\text{O}_4$  (Fig. 2c), two main peaks are observed at binding energies of about 780 and 796 eV, with the shake-up satellite (denoted as Sta.) structure at 786.46 and 803.02. After Gaussian fitting, the peaks of Co 2p<sub>3/2</sub> and Co 2p<sub>1/2</sub> can be further fitted to two peaks. Peaks centered at 780.10 and 795.50 eV are ascribed to  $\text{Co}^{2+}$ , while that of at 781.88 and 797.26 eV are ascribed to  $\text{Co}^{3+}$  [40,41]. Moreover, the analysis results shows that the molar ratio of  $\text{Co}^{2+}/\text{Co}^{3+}$  in  $\text{CoO}@\text{MnCo}_2\text{O}_4$  is 1:6.49, which is close to the theoretical molar ratio (is about 1:6.31) of the as-synthesized composite. The O1s peaks (Fig. 2d) at binding energy of 529.85 and 531.65 eV are attributed to  $\text{O}^{2-}$  forming oxide formation with Co and Mn elements. The high binding energy component located at 532.97 eV may be attributed to the adsorbed  $\text{H}_2\text{O}$  or surface hydroxyl group [30,42].

Fig. 3a displays the Nyquist plots of  $\text{MnCo}_2\text{O}_4$ ,  $\text{CoO}$  and  $\text{CoO}@\text{MnCo}_2\text{O}_4$  materials. In general, a smaller arc radius implies higher efficiency in charge transfer [43]. Clearly, the arc radius of  $\text{CoO}@\text{MnCo}_2\text{O}_4$  heterojunction was smaller than that of  $\text{MnCo}_2\text{O}_4$  or  $\text{CoO}$ , implying  $\text{CoO}@\text{MnCo}_2\text{O}_4$  possessed of a higher interfacial charge transfer and a more effective separation of carriers. The lower electron transfer resistance in  $\text{CoO}@\text{MnCo}_2\text{O}_4$  could be ascribed to construct  $\text{CoO}@\text{MnCo}_2\text{O}_4$  p-n junction. In addition, the photocurrent response of  $\text{CoO}@\text{MnCo}_2\text{O}_4$  sample is higher than the pure  $\text{MnCo}_2\text{O}_4$  or  $\text{CoO}$ .

(Fig. 3b). The result reflects a more efficient separation and longer lifetimes of photo-excited  $e^-/h^+$  pairs of  $\text{CoO}@\text{MnCo}_2\text{O}_4$  hybrid [44]. This may attribute to the electric field on the interface between  $\text{MnCo}_2\text{O}_4$  and  $\text{CoO}$ , further confirming that the heterojunction was fabricated between  $\text{MnCo}_2\text{O}_4$  and  $\text{CoO}$  through deposition of  $\text{CoO}$  on the surface of  $\text{MnCo}_2\text{O}_4$ .

Fig. 4a displays the UV-vis diffuse reflectance spectra of  $\text{MnCo}_2\text{O}_4$ ,  $\text{CoO}$  and  $\text{CoO}@\text{MnCo}_2\text{O}_4$  composite. Obviously, the  $\text{CoO}@\text{MnCo}_2\text{O}_4$  hybrid displays enhanced absorption in the visible region caused by the interactions between  $\text{MnCo}_2\text{O}_4$  and  $\text{CoO}$  (via the formed a p-n junction). The derived band gaps can be obtained by the Kubelka-Munk theorem (inset of Fig. 4a). The obtained corresponding  $E_g$  for samples are 2.36 eV ( $\text{CoO}$ ), 1.69 eV ( $\text{MnCo}_2\text{O}_4$ ), and 1.91 eV ( $\text{CoO}@\text{MnCo}_2\text{O}_4$ ). To estimate the conduction band edge potentials, the flat band potentials of the samples were investigated by Mott-Schottky plots (Fig. 4b–d). It is worth noting that  $\text{CoO}$  is confirmed as a p-type semiconductor due to the negative slope in the Mott-Schottky plot (Fig. 4b), while  $\text{MnCo}_2\text{O}_4$  is identified as an n-type semiconductor based on the Mott-Schottky plot (Fig. 4c) [3]. When the p-n junction was constructed, Mott-Schottky plots of  $\text{CoO}@\text{MnCo}_2\text{O}_4$  hybrid presents an inverted “V-shape” (Fig. 4d). In general, the  $E_{VB}$  for p-type semiconductors is very close to the flat-band potential, while the  $E_{CB}$  for n-type semiconductors is very close to the flat-band potential value [45–48]. That is, the flat-band potential is 0.1–0.3 eV higher than the conduction band (CB) potential in the n-type semiconductor; while that is 0.1–0.3 eV lower than the valence band potential in the p-type semiconductor [49–51]. As Fig. 4b, c shown, the  $E_{VB}$ ,  $\text{CoO}$  and the  $E_{CB}$ ,  $\text{MnCo}_2\text{O}_4$  could be confirmed to be 0.64 (0.84 eV vs. NHE) and -0.68 eV (-0.48 eV vs. NHE), respectively. Therefore, the  $E_{VB}$ ,  $\text{CoO}$  and the  $E_{CB}$ ,  $\text{MnCo}_2\text{O}_4$  could be estimated to be 0.94 eV and -0.58 eV. Based on the formula  $E_{CB} = E_{VB} - E_g$  [52], the corresponding  $E_{CB}$  of  $\text{CoO}$  and  $E_{VB}$  of  $\text{MnCo}_2\text{O}_4$  will occur at about -1.42 and 1.11 eV, respectively.

### 3.2. Photocatalytic activity

The photocatalytic activity of as-fabricated  $\text{CoO}@\text{MnCo}_2\text{O}_4$  hybrid was evaluated by catalytic TC in aqueous solution under visible light irradiation (Fig. 5a). Obviously, the  $\text{CoO}@\text{MnCo}_2\text{O}_4$  hybrid displayed an enhanced photocatalytic performance compared to the pristine  $\text{MnCo}_2\text{O}_4$  or  $\text{CoO}$ . The degradation efficiency is ca. 86%. The inset of Fig. 5a shows the changes of absorbance of TC during the

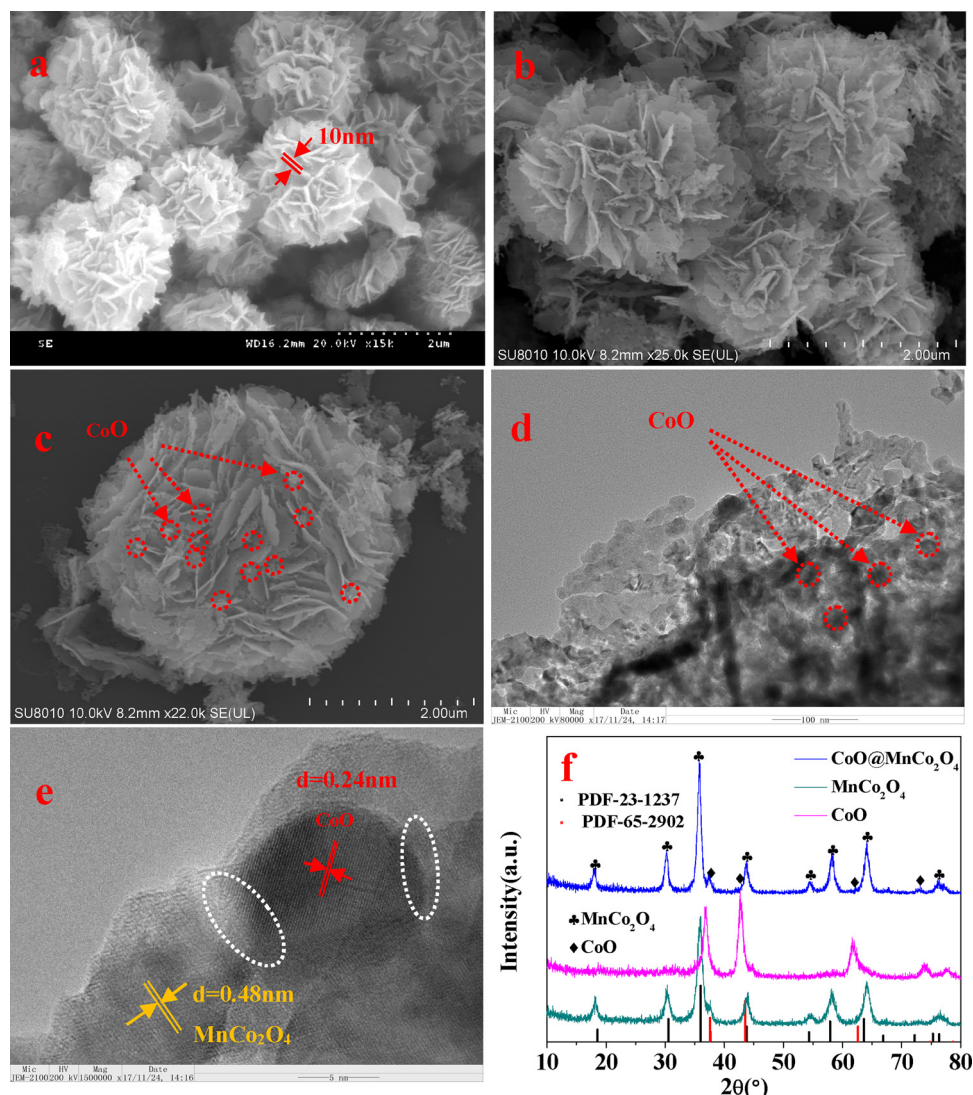


**Fig. 1.** The SEM image of (a)  $\text{MnCo}_2\text{O}_4$ , (b, c)  $\text{CoO}@\text{MnCo}_2\text{O}_4$ , (d) TEM image of and HRTEM image of  $\text{CoO}@\text{MnCo}_2\text{O}_4$  and (f) XRD patterns of the as-prepared samples.

photocatalytic process. It can be found that the intensity of the characteristic peak decreases with the increase of visible light illumination time. A linear relation of  $\ln(C_0/C)$  vs reaction time was obtained (Fig. 5b), implying that the reaction can be considered as a pseudo-first-order reaction. The corresponding apparent kinetic rate constant ( $k$ ) value of  $\text{CoO}@\text{MnCo}_2\text{O}_4$  hybrid was calculated to be  $0.017 \text{ min}^{-1}$ , which is over 5.7 and 4.3 times higher than that of  $\text{MnCo}_2\text{O}_4$  ( $0.003 \text{ min}^{-1}$ ) and  $\text{CoO}$  ( $0.004 \text{ min}^{-1}$ ). Furthermore, the TOC removal ratio was evaluated using TOC analyzer. The result shows that the maximum TOC removal efficiency of TC reached 88.94% after 120 min.

Additionally, the photocatalytic performance of as-fabricated  $\text{CoO}@\text{MnCo}_2\text{O}_4$  hybrid was also evaluated by catalytic Cr (VI) reduction (Fig. 6a). It is found that pure  $\text{MnCo}_2\text{O}_4$  and  $\text{CoO}$  showed a weak performance for photocatalytic Cr (VI) reduction, corresponding reduction efficiency is about 49.17% and 30.25% within 120 min, respectively. The performance is greatly enhanced after forming  $\text{CoO}@\text{MnCo}_2\text{O}_4$  p-n junction. The reduction efficiency of Cr (VI) reached to about 91.90% over  $\text{CoO}@\text{MnCo}_2\text{O}_4$  hybrid. As the Fig. 6b shown, the reaction rate constant  $k$  of  $\text{CoO}@\text{MnCo}_2\text{O}_4$  is  $0.021 \text{ min}^{-1}$  for the photocatalytic Cr (VI) reduction, about 3.5 and 7.0 times that of  $\text{CoO}$  ( $0.006 \text{ min}^{-1}$ ) and  $\text{CoMn}_2\text{O}_4$  ( $0.003 \text{ min}^{-1}$ ).

The valence state of Cr adsorbed on the  $\text{CoO}@\text{MnCo}_2\text{O}_4$  was investigated after photocatalytic reduction. The  $\text{CoO}@\text{MnCo}_2\text{O}_4$  was

collected after irradiation and the surface composition was characterized using XPS. The peaks located at 576.20 and 586.50 eV ascribable to  $\text{Cr}2\text{p}_{3/2}$  and  $\text{Cr}2\text{p}_{1/2}$  of Cr(III), while that at 579.53 and 586.01 eV corresponds to  $\text{Cr}2\text{p}_{3/2}$  and  $\text{Cr}2\text{p}_{1/2}$  orbitals, regarding as the signals of Cr (VI) (Fig. 6c) [53–55]. It can be found that partially of Cr (VI) inverted to Cr (III) after irradiation 60 min (Fig. 6c-I). When the illumination time increased to 120 min (Fig. 6c-II), the peaks of the Cr (VI) was not observed, implying that the Cr (VI) completely converted to Cr (III).

To investigate the effect of light source on photocatalytic activity, the experiments of photodegradation of TC and Cr(VI) on the samples was measured under the UV-vis irradiation without using the 420 nm filter. As Fig. 5c shown, a slight increase in degradation efficiency was observed, increased by 4.95% for TC degradation (for Cr (VI) reduction, increased by 2.16%). Compared to  $\text{TiO}_2$  (P25), the well-known benchmark photocatalyst,  $\text{CoO}@\text{MnCo}_2\text{O}_4$  hybrids displayed superior photocatalytic performance under both visible and UV-vis illumination in the identical condition. The result unambiguously implies that  $\text{CoO}@\text{MnCo}_2\text{O}_4$  could be a catalyst with boosting solar light photocatalytic activity.

As illustrated in Fig. 5d, the total removal effect of Cr (VI)/TC (96.07% and 94.02%, respectively) in mixture system is further enhancement under the UV-vis illumination. The absorbance of mixture

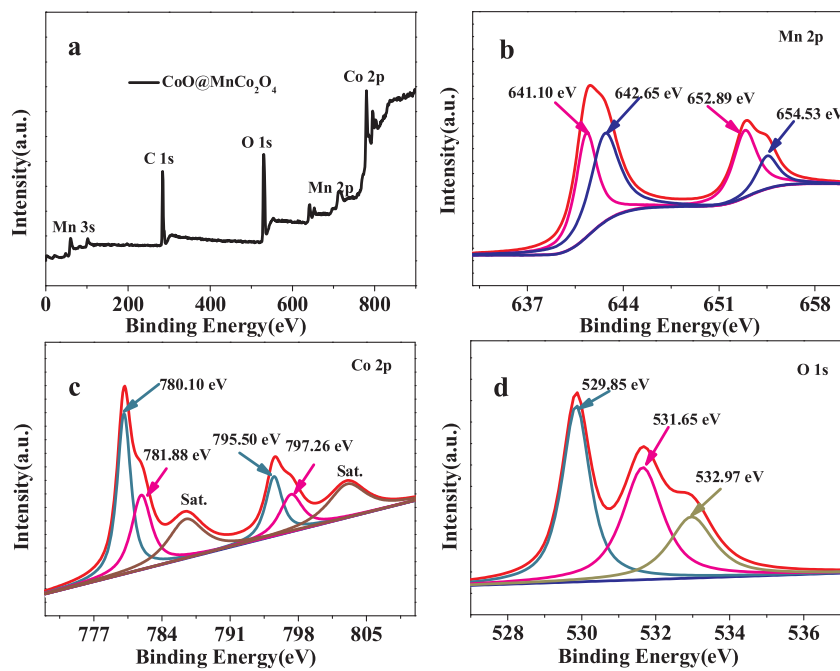


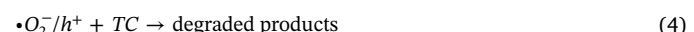
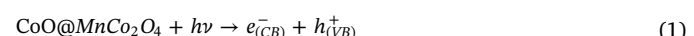
Fig. 2. XPS spectra of (a) the survey, (b) Mn 2p, (c) Co 2p and (d) O 1s in the as-prepared CoO@MnCo<sub>2</sub>O<sub>4</sub> hybrid.

was also recorded by UV-vis spectrophotometer (inset of Fig. 5d). The high photocatalytic efficiency mainly attributed to the synergistic effect during the PCR of Cr (VI) and PCO of TC. During the mixture reaction system, Cr (VI) serves as an electron acceptor, consuming the photo-excited CB electrons; and at the same time, TC acts as an electron donor, reacting with the photo-generated holes, which further improve the separation rate of  $e^-/h^+$  pairs. The similar phenomenon has been also reported in the previous literatures.[1,55] According to the experiment results, simultaneous PCR of Cr (VI) and PCO of TC over CoO@MnCo<sub>2</sub>O<sub>4</sub> is also feasibility.

### 3.3. Photocatalytic mechanism

According to the estimated band position of MnCo<sub>2</sub>O<sub>4</sub> and CoO (Fig. 3b), the possible mechanism for enhanced photocatalytic performance of CoO@MnCo<sub>2</sub>O<sub>4</sub> can be concluded (Scheme 2). When CoO@MnCo<sub>2</sub>O<sub>4</sub> hybrid was exposed to visible light, both of MnCo<sub>2</sub>O<sub>4</sub> and CoO can be excited, generating the electrons and holes ( $e^-/h^+$  pairs). The electrons in the  $E_{CB}$  of CoO can easily transfer to the  $E_{CB}$  of MnCo<sub>2</sub>O<sub>4</sub> with the assistance of the internal electric field owing to formation a stable p-n junction in CoO@MnCo<sub>2</sub>O<sub>4</sub> composites. Analogously, this mechanism readily enables the migration of holes from the  $E_{VB}$  of MnCo<sub>2</sub>O<sub>4</sub> to CoO. For TC mineralization system, the electrons accumulated in the  $E_{CB}$  of MnCo<sub>2</sub>O<sub>4</sub> can react with dissolved O<sub>2</sub>

generating  $\cdot O_2^-$ , because the  $E(O_2/\cdot O_2^-)$  (−0.33 eV vs. NHE) [56] is more positive than the  $E_{CB}$  of MnCo<sub>2</sub>O<sub>4</sub> (−0.58 eV). Subsequently, the  $\cdot O_2^-$  and the oxidative holes leaving in the  $E_{VB}$  of CoO directly mineralize TC. In the reaction of photocatalytic reduction Cr (VI), the conduction band potential of MnCo<sub>2</sub>O<sub>4</sub> is −0.58 eV vs NHE, which is more negative than the standard reduction potential of Cr (VI)/Cr (III) (1.33 eV vs NHE), indicating photocatalytic reduction of Cr (VI) is thermodynamically allowed [57,58]. Therefore, the electrons accumulated in the  $E_{CB}$  of MnCo<sub>2</sub>O<sub>4</sub> can reduce Cr (VI) to Cr (III). Therefore, the improved separation of photogenerated charges carriers at the interface between CoO and MnCo<sub>2</sub>O<sub>4</sub> is mainly responsible for the remarkable photocatalytic activity. On the basis of analysis above-mentioned, the corresponding photocatalytic reactions may be expressed in the following Eqs. (1)–(4) [59,60]:



It was notable that the unique hierarchical 3D structure of CoO@MnCo<sub>2</sub>O<sub>4</sub> not only facilitates the diffusion of contaminant as well as catalytic sites per unit mass but also exhibits high light-harvesting

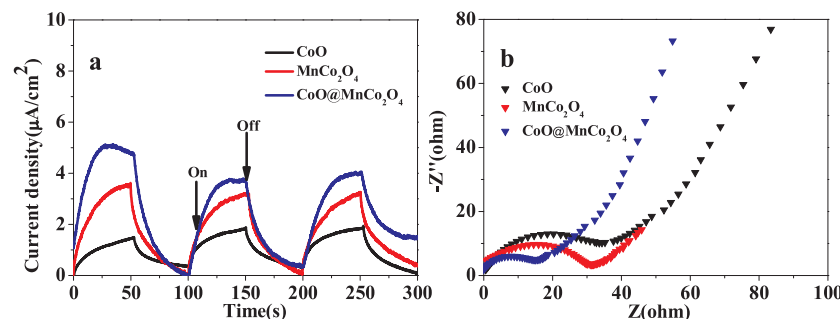


Fig. 3. (a) The periodic on/off photocurrent response at 0.2 V bias potential vs. Ag/AgCl, and (b) EIS Nyquist plots at 0.1 V bias potential vs. Ag/AgCl of different samples (0.1 mol L<sup>-1</sup> Na<sub>2</sub>SO<sub>4</sub> aqueous solutions).

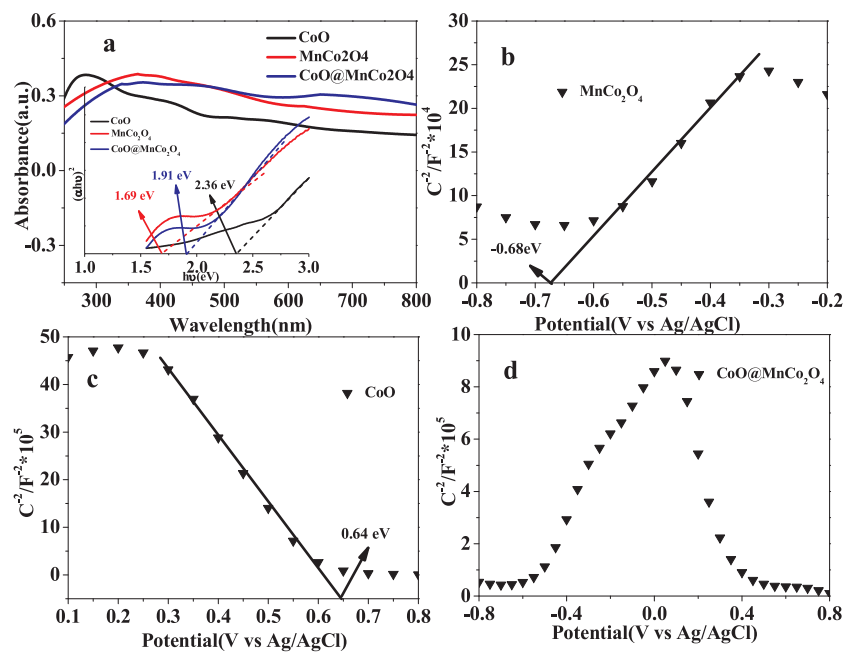


Fig. 4. (a) UV-vis diffuse reflectance spectra of samples and the Mott-Schottky plots of (b) MnCo<sub>2</sub>O<sub>4</sub> (c) CoO and (d) CoO@MnCo<sub>2</sub>O<sub>4</sub>.

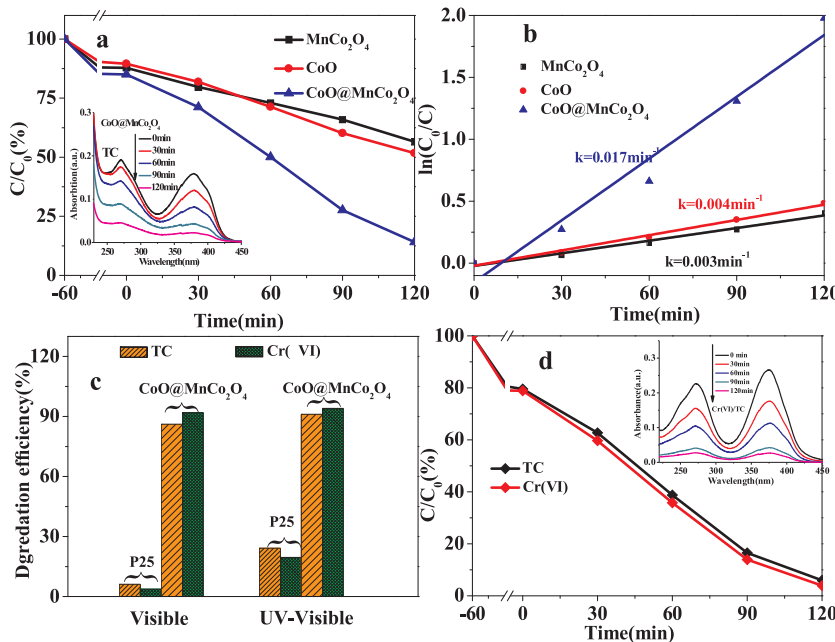


Fig. 5. (a) Photocatalytic degradation of TC of different samples under visible-light irradiation, (b) the corresponding first-order plots, (c) The effect of light source on photocatalytic degradation of TC and reduction of Cr (VI) over different catalyst and (d) Simultaneous photocatalysis of the TC and Cr (VI) over CoO@MnCo<sub>2</sub>O<sub>4</sub> under. UV-vis.

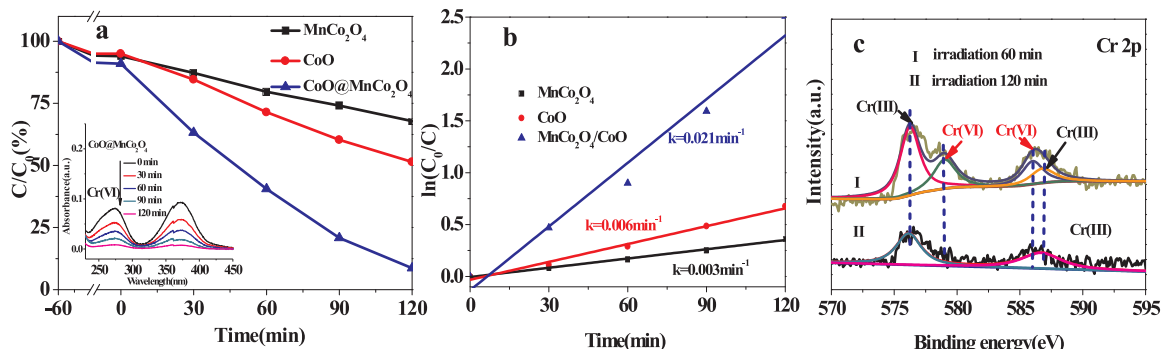
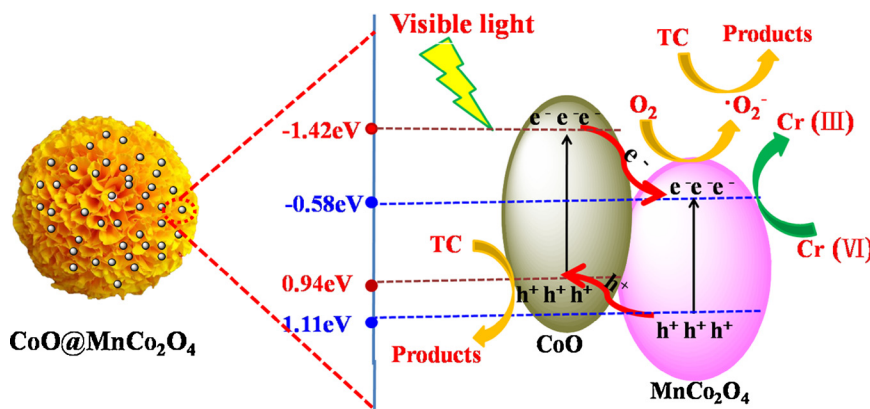
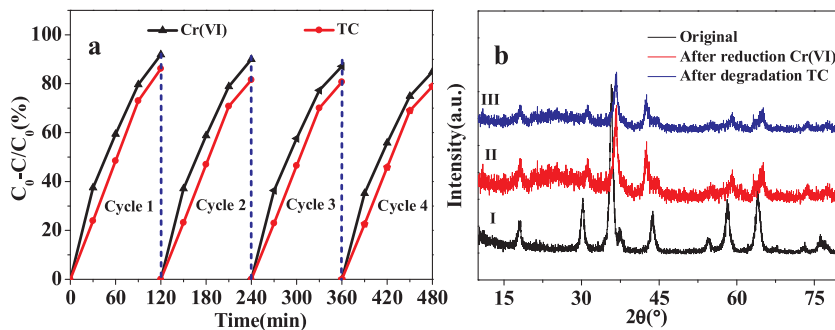


Fig. 6. (a) Photocatalytic reduction of Cr (VI) of different samples under visible-light irradiation, (b) the corresponding first-order plots, and (c) XPS spectra of Cr 2p.



**Scheme 2.** Proposed photocatalytic reaction processes and charge transfer of  $\text{CoO}@\text{MnCo}_2\text{O}_4$ .



**Fig. 7.** (a) Cycling experiments for photocatalytic reduction of Cr (VI) and oxidation of TC over the prepared  $\text{CoO}@\text{MnCo}_2\text{O}_4$ , and (b) The XRD patterns of  $\text{CoO}@\text{MnCo}_2\text{O}_4$  before and after cyclic test.

capabilities by multiple scattering, which further promote the photocatalytic reaction efficiency. Then again,  $\text{MnCo}_2\text{O}_4$  and  $\text{CoO}$  can achieve better photocatalytic performance through a reinforcement or modification with each other and a p-n junction formed.

#### 3.4. Stability

The reusability of the catalysts was investigated via the cycle experiments using  $\text{CoO}@\text{MnCo}_2\text{O}_4$  hybrid photocatalyst. For each recycling test,  $\text{CoO}@\text{MnCo}_2\text{O}_4$  was cleaned thrice using deionized water and ethanol, respectively. As exhibited in Fig. 7a, the catalytic performance of  $\text{CoO}@\text{MnCo}_2\text{O}_4$  was a slight decrease after testing more than four times, indicating that the  $\text{CoO}@\text{MnCo}_2\text{O}_4$  composite is a conveniently reusable photocatalyst. Moreover, the structural stability was further confirmed by the XRD (Fig. 7b). Clearly, there is no noticeable change observed in the XRD pattern before and after the photocatalytic processes. Therefore, the present  $\text{CoO}@\text{MnCo}_2\text{O}_4$  hybrid can be considered to be a stable and recyclable visible-light-driven photocatalyst.

#### 4. Conclusions

In summary, the hierarchical 3D flower-like  $\text{CoO}@\text{MnCo}_2\text{O}_4$  p-n heterojunction was successfully fabricated with the anchoring of  $\text{CoO}$  nanoparticles on the surface of  $\text{MnCo}_2\text{O}_4$ . The as-prepared  $\text{CoO}@\text{MnCo}_2\text{O}_4$  composites displayed an improved photocatalytic performance for PCR of Cr (VI) and PCO of TC than pure  $\text{MnCo}_2\text{O}_4$  and  $\text{CoO}$  under visible light irradiation. The enhanced photocatalytic activity might be attributed to the fast charge separation by the inner electric field through the formation of a p-n heterojunction between  $\text{MnCo}_2\text{O}_4$  and  $\text{CoO}$  as well as the complex structure. The present study provides a reference to construct new p-n junction photocatalysts for other environmental remediation applications.

#### Acknowledgement

This work was financially supported by the National Nature Science Foundation of China (No. NSFC51672116).

#### References

- [1] Y. Deng, L. Tang, G. Zeng, Z. Zhu, M. Yan, Y. Zhou, J. Wang, Y. Liu, J. Wang, *Appl. Catal. B: Environ.* 203 (2017) 343–354.
- [2] Y. He, L. Zhang, M. Fan, X. Wang, M.L. Walbridge, Q. Nong, Y. Wu, L. Zhao, *Sol. Energy Mater. Sol. Cells* 137 (2015) 175–184.
- [3] X.J. Wen, C.G. Niu, L. Zhang, G. Zeng, *ACS Sustain. Chem. Eng.* 5 (2017) 5134–5147.
- [4] F. Chen, Q. Yang, X. Li, G. Zeng, D. Wang, C. Niu, J. Zhao, H. An, T. Xie, Y. Deng, *Appl. Catal. B: Environ.* 200 (2017) 330–342.
- [5] F. Chen, Q. Yang, J. Sun, F. Yao, S. Wang, Y. Wang, X. Wang, X. Li, C. Niu, D. Wang, *ACS Appl. Mater. Interfaces* 8 (2016) 32887–32900.
- [6] X. Yang, R. Li, Y. Wang, K. Wu, S. Chang, H. Tang, *Ceram. Int.* 42 (2016) 13411–13420.
- [7] T. Yang, J. Peng, Y. Zheng, X. He, Y. Hou, L. Wu, X. Fu, T. Yang, J. Peng, Y. Zheng, *Appl. Catal. B: Environ.* 221 (2018) 223–234.
- [8] A.G. Shiravizadeh, R. Yousefi, S.M. Elahi, S.A. Sebt, *Phys. Chem. Chem. Phys.* 19 (2017) 18089–18098.
- [9] B. Liu, X. Li, Q. Zhao, Y. Hou, G. Chen, J. Mater. Chem. A 5 (2017) 8909–8915.
- [10] X. Yang, H. Cui, Y. Li, J. Qin, R. Zhang, H. Tang, *ACS Catal.* 3 (2013) 363–369.
- [11] X.L. Zheng, C.T. Dinh, F.P. de Arquer, B. Zhang, M. Liu, O. Vozny, Y.Y. Li, G. Knight, S. Hoogland, Z.H. Lu, *Small* 12 (2016) 3181–3188.
- [12] K. Xiong, K. Wang, L. Chen, X. Wang, Q. Fan, J. Courtois, Y. Liu, X. Tuo, M. Yan, *Nano-Micro Lett.* 10 (2018) 17.
- [13] H. Yang, X.Y. Li, Q.D. Zhao, Q. Xie, G.H. Chen, *Environ. Sci. Technol.* 44 (2010) 5098–5103.
- [14] T. Li, Y. Lv, J. Su, Y. Wang, Q. Yang, Y. Zhang, J. Zhou, L. Xu, D. Sun, Y. Tang, *Adv. Sci.* 4 (2017) 1700226.
- [15] Y. Qi, B. Liu, L. Zhang, Y. Huo, L. Li, H. Xie, C. Wang, Z.M. Su, Y. Qi, B. Liu, *J. Mater. Chem. A* (2017) 21994–22003.
- [16] J. Mondal, K. Dhanalaxmi, R. Yadav, S.K. Kundu, V. Amoli, A.K. Sinha, R.B. Mahipal, *Chemistry* 44 (2016) 15639–15644.
- [17] B. Wang, R. Li, Z. Zhang, W. Zhang, X. Yan, X. Wu, G. Cheng, R. Zheng, *J. Mater. Chem. A* 5 (2017) 14415–14421.
- [18] Y. Li, X. Hou, Y. Li, Q. Ru, S. Wang, S. Hu, K.H. Lam, *Electron. Mater. Lett.* 13 (2017) 427–433.

[19] Z. Luo, E. Irtem, M. Ibáñez, R. Nafria, S. Martí-Sánchez, A. Genç, M.M. De, Y. Liu, D. Cadavid, J. Llorca, *ACS Appl. Mater. Interfaces* 8 (2016) 17435–17444.

[20] J.G. Kim, S.H. Lee, Y. Kim, W.B. Kim, *ACS Appl. Mater. Interfaces* 5 (2013) 11321–11328.

[21] X. Wu, Y. Xiang, Q. Peng, X. Wu, Y. Li, F. Tang, R. Song, Z. Liu, Z. He, X. Wu, *J. Mater. Chem. A* 5 (2017) 17990–17997.

[22] X. Gao, H. Zhang, Q. Li, X. Yu, Z. Hong, X. Zhang, C. Liang, Z. Lin, *Angew. Chem.* 55 (2016) 6290–6294.

[23] Z.Q. Liu, Q.Z. Xu, J.Y. Wang, N. Li, S.H. Guo, Y.Z. Su, H.J. Wang, J.H. Zhang, S. Chen, *Int. J. Hydrogen Energy* 38 (2013) 6657–6662.

[24] Z.Q. Liu, H. Cheng, N. Li, T.Y. Ma, Y.Z. Su, *Adv. Mater.* 28 (2016) 3777–3784.

[25] H. Cheng, C.Y. Su, Z.Y. Tan, S.Z. Tai, Z.Q. Liu, *J. Power Sources* 357 (2017) 1–10.

[26] W. Kang, Y. Tang, W. Li, Z. Li, X. Yang, J. Xu, C.S. Lee, *Nanoscale* 6 (2014) 6551–6556.

[27] S. Wang, Y. Hou, X. Wang, *ACS Appl. Mater. Interfaces* 7 (2015) 4327–4335.

[28] S.M.A. Shibli, P.S. Arun, A.V. Raj, *RSC Adv.* 5 (2015) 19393–19399.

[29] Y. Zhai, H. Mao, P. Liu, X. Ren, L. Xu, Y. Qian, *J. Mater. Chem. A* 3 (2015) 16142–16149.

[30] S. Liu, K.S. Hui, K.N. Hui, J.M. Yun, K.H. Kim, *J. Mater. Chem. A* 4 (2016) 8061–8071.

[31] C. Xiao, S. Li, X. Zhang, D. Macfarlane, *J. Mater. Chem. A* 5 (2017) 7825–7832.

[32] S. Yuvaraj, A. Vignesh, S. Shanmugam, R.K. Selvan, *Int. J. Hydrogen Energy* 41 (2016) 15199–15207.

[33] X. Chen, R. Li, J. Wang, Q. Zhong, Y. Bu, *Chemistryselect* 1 (2016) 2159–2162.

[34] L. Zhang, Y. Hu, J. Zheng, *J. Mater. Chem. A* 5 (2017) 18664–18673.

[35] Y. Li, L. Lan, Z. Shi, Q. Zhang, Y. Yang, S. Wu, X. Zhao, *J. Mater. Chem. A* 6 (2018) 7194–7205.

[36] S. Ma, L. Sun, L. Cong, X. Gao, C. Yao, X. Guo, L. Tai, P. Mei, Y. Zeng, H. Xie, *J. Phys. Chem. C* 117 (2013) 25890–25897.

[37] Z. Mao, J. Chen, Y. Yang, D. Wang, L. Bie, B.D. Fahlman, *ACS Appl. Mater. Interfaces* 9 (2017) 12427–12435.

[38] M. Zeng, Y. Li, F. Liu, Y. Yang, M. Mao, X. Zhao, *Appl. Catal. B: Environ.* 200 (2017) 521–529.

[39] J. Hou, Y. Li, M. Mao, L. Ren, X. Zhao, *ACS Appl. Mater. Interfaces* 6 (2014) 14981–14987.

[40] X. Cao, J. Wu, C. Jin, J. Tian, P. Strasser, R. Yang, *ACS Catal.* 5 (2015) 4890–4896.

[41] X. Huang, L. Liu, H. Gao, W. Dong, M. Yang, G. Wang, *Green Chem.* 19 (2016) 769–777.

[42] C. Huang, W. Ye, Q. Liu, X. Qiu, *ACS Appl. Mater. Interfaces* 6 (2014) 14469–14476.

[43] W. Zou, Y. Shao, Y. Pu, Y. Luo, J. Sun, K. Ma, C. Tang, F. Gao, L. Dong, *Appl. Catal. B: Environ.* 218 (2017) 51–59.

[44] D.A. Reddy, H. Park, R. Ma, D.P. Kumar, M. Lim, T.K. Kim, *ChemSusChem* 10 (2017) 1563–1570.

[45] X. Zong, H. Yan, G. Wu, G. Ma, F. Wen, L. Wang, C. Li, *J. Am. Chem. Soc.* 130 (2008) 7176–7177.

[46] J.S. Jang, H.G. Kim, J.S. Lee, *Catal. Today* 185 (2012) 270–277.

[47] H. Chen, W. Leng, Y. Xu, *J. Phys. Chem. C* 118 (2014) 9982–9989.

[48] U.A. Joshi, P.A. Maggard, *J. Phys. Chem. Lett.* 3 (2012) 1577–1581.

[49] F. Guo, W. Shi, H. Wang, M. Han, H. Li, H. Huang, Y. Liu, Z. Kang, *Catal. Sci. Technol.* 7 (2017) 3325–3331.

[50] B.A. Pinaud, Z. Chen, D.N. Abram, T.F. Jaramillo, *J. Phys. Chem. C* 115 (2011) 11830–11838.

[51] J. Yang, D. Chen, Y. Zhu, Y. Zhang, Y. Zhu, *Appl. Catal. B: Environ.* 205 (2016) 228–237.

[52] X.J. Wen, C. Zhang, C.G. Niu, L. Zhang, G.M. Zeng, X.G. Zhang, *Catal. Commun.* 90 (2017) 51–55.

[53] B. Nanda, A.C. Pradhan, K.M. Parida, *Chem. Eng. J.* 316 (2017) 1122–1135.

[54] D. Lu, W. Chai, M. Yang, P. Fang, W. Wu, B. Zhao, R. Xiong, H. Wang, *Appl. Catal. B: Environ.* 190 (2016) 44–65.

[55] Q. Yuan, C. Lang, X. Miao, H. Jie, S.L. Luo, C.T. Au, S.F. Yin, *Chem. Eng. J.* 255 (2014) 394–402.

[56] Z. Li, T. Dong, Y. Zhang, L. Wu, J. Li, Xuxu Wang, X. Fu, *J. Phys. Chem. C* 111 (2007) 4727–4733.

[57] J. Liu, X. Jin, Y. Shi, M. Qiao, *J. Nanotechnol.* (2015) 1–8.

[58] Xiangwen, Jiefu Huaqiang, *Nano Res.* 4 (2011) 470–482.

[59] J. Yu, S. Zhuang, X. Xu, W. Zhu, B. Feng, J. Hu, *J. Mater. Chem. A* 3 (2014) 1199–1207.

[60] D.K. Padhi, T.K. Panigrahi, K.M. Parida, S.K. Singh, P.M. Mishra, *ACS Sustain. Chem. Eng.* 5 (2017) 10551–10562.